ACS Energy LETTERS

Open Access

http://pubs.acs.org/journal/aelccp

Letter

Bimodal Composite Cathodes Advancing the Chemo-Mechanical Integrity and Kinetics for All-Solid-State Batteries

Hyeonseong Oh,[¶] Uigyeong Jeong,[¶] Junhyeok Choi, Jaejin Lim, Jun Tae Kim, Hyeon-Ji Shin, Jong-yeon Im, Hyun-Woo Gong, Jae-Pyoung Ahn, Yong Min Lee, Jongsoon Kim, Junyoung Mun, Kyung Yoon Chung, Si Hyoung Oh, Jong-Won Lee,* Sang-Young Lee,* and Hun-Gi Jung*

Cite This: *ACS Energy Lett.* 2026, 11, 2103−2114

Read Online

ACCESS | Metrics & More | Article Recommendations | Supporting Information

ABSTRACT: All-solid-state batteries employing sulfide solid electrolytes promise high energy density and safety but suffer from poor cycling stability and rate performance due to fundamental shortcomings in composite electrode architectures. To address challenges, this study introduces bimodal composite cathodes formed by blending large polycrystalline and small single-crystalline cathode active materials (CAMs). This bimodal configuration optimizes particle packing and porosity, thereby reducing ionic tortuosity and enhancing Li^+ transport. At an extreme CAM loading of 90 wt%, a bimodal composition with a 7:3 mass ratio of polycrystalline to single-crystalline CAM exhibited enhanced rate performance and 87.8% capacity retention after 200 cycles, outperforming unimodal composite cathodes. Distribution-of-relaxation-times analysis, operando X-ray diffraction, operando electrochemical pressiometry, and three-dimensional simulations revealed that the enhanced mechanical performance of densely packed electrode structures originates not from stress relaxation but from uniform stress dispersion. These findings establish a comprehensive framework for advancing the design and optimization of complex composite cathodes.

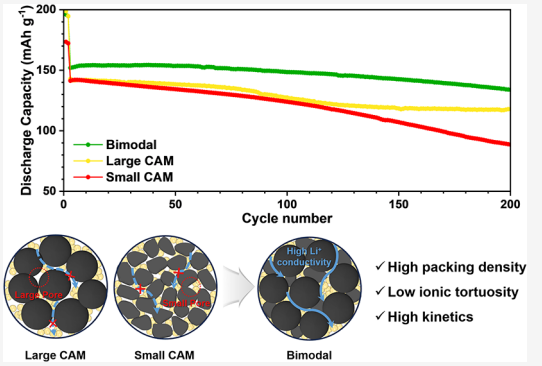

Lithium-ion batteries (LIBs) with high energy density have made remarkable progress over the past decade, enabling longer driving ranges for electric vehicles and extended operating times for portable electronic devices.[1] However, the intrinsic instability of liquid electrolytes used in conventional LIBs, combined with the structural instability of layered oxide cathode active materials (CAMs), has raised serious concerns regarding their long-term safety and reliability.[2−5] To address these safety limitations and the plateau in energy density, all-solid-state batteries (ASSBs) incorporating solid electrolytes have emerged as promising next-generation energy storage systems.[6−9] Among the various solid electrolytes explored, sulfide-based solid electrolytes (SSEs) are considered particularly promising for commercial ASSB applications due to their ionic conductivities comparable to those of liquid electrolytes and their relatively facile processability.[10−15] Paradoxically, however, replacing liquid electrolytes with SSEs has often resulted in incomplete utilization of the theoretical specific capacity of conventional CAMs. This limitation arises primarily from the fundamental challenges of composite electrode design in ASSBs. Interfaces formed through the mechanical mixing of CAMs and SSEs frequently exhibit poor interfacial contact.[16] Furthermore, the electrochemical instability of SSEs leads to interfacial degradation, which significantly increases overall cell impedance, thereby diminishing reversible capacity and cycling stability.[17] In addition, high porosity within the electrode exacerbates nonhydrostatic stress generation during cycling—an effect far more pronounced in ASSBs than in LIBs—causing mechanical deterioration and reduced long-term stability.[18,19] To overcome these challenges, various strategies have been proposed, including the development of SSEs with enhanced ductility and electrochemical stability, optimization of SSE particle size, and the incorporation of functionalized binders to improve electrode mechanical integrity.[20−24] Collectively, these studies underscore that achieving reliable and high-performance ASSBs requires not only advances in materials design but also electrode-level engineering. In this context, the choice of CAM is as critical as that of SSE in determining ASSB performance.[25] Conventional large polycrystalline CAMs used in liquid-electrolyte-based LIBs and small single-crystalline CAMs introduced more recently each exhibit distinct advantages and drawbacks.[26] The outstanding cycling stability

Received: November 24, 2025
Revised: January 9, 2026
Accepted: January 13, 2026
Published: January 23, 2026

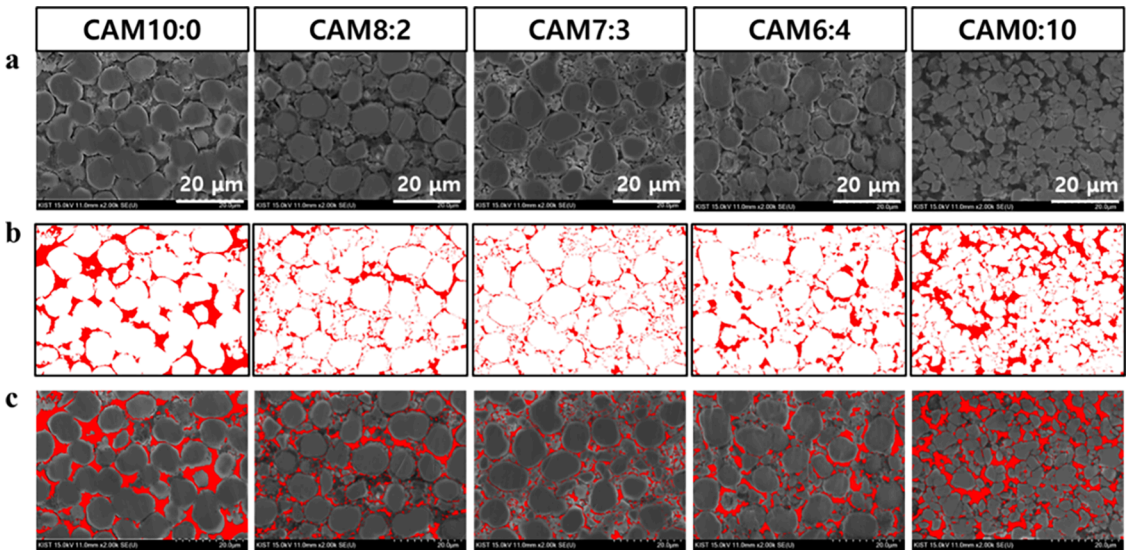

Figure 1. Two-dimensional image characterization of composite cathodes. (a) Cross-sectional scanning electron microscopy (SEM) images of each composite cathode (scale bars: 20 μm). (b) Pore size and distribution within the composite cathodes, where the red regions represent pore structures. (c) Composite cathode−pore overlay images. Each column corresponds to one type of composite cathode.

of single-crystalline CAMs—primarily attributed to their superior mechanical robustness—has attracted considerable attention, positioning them as promising candidates for ASSB cathodes.[27] Their small particle size also enables short and efficient Li^+ diffusion paths, resulting in excellent rate performance.[28] Conversely, polycrystalline CAMs remain attractive due to their cost-effective manufacturability and high packing density, which contribute to elevated volumetric energy density.[29−31] Moreover, appropriately large particle sizes in CAMs can yield electrochemical advantages by providing favorable size compatibility with SSE particles.[32,33] In this study, unimodal and bimodal composite cathodes were fabricated using large polycrystalline $LiNi_{0.88}Co_{0.10}W_{0.01}Al_{0.01}O_2$ (NCWA) and small single-crystalline $LiNi_{0.82}Co_{0.13}Mn_{0.05}O_2$ (NCM), and their electrochemical performances were systematically compared. To achieve high volumetric energy density, the CAM content was fixed at 90 wt % of the total composite cathode—one of the highest reported in recent literature. ASSB performance was evaluated using $Li_4Ti_5O_{12}$ (LTO) as the anode, selected for its negligible volume change during lithiation and delithiation.[34] From a materials perspective, large polycrystalline CAMs with improved mechanical properties achieved through transition metal doping demonstrated partially viable performance in ASSBs.[35,36] However, their inherent rate limitations could not be mitigated solely through compositional optimization. This work therefore introduces an electrode-level engineering strategy based on bimodal composite cathodes, wherein NCM particles occupy the interstitial voids between NCWA particles, effectively reducing overall electrode porosity. The optimized CAM arrangement and its influence on electrode electrochemistry and mechanical integrity were analyzed through comprehensive post-mortem electrochemical, structural, and mechanical characterizations. In particular, operando electrochemical pressiometry and three-dimensional simulations were employed to elucidate the mechanisms by which bimodal configurations enhance performance. Finally, the study highlights the critical role of porosity control in the rational design of high-performance composite cathodes for ASSBs.

It is well established that mixing powders with different particle sizes enhances packing density, but ASSB composite cathodes comprise not only CAMs but also SSEs and conductive carbon additives (CC).[37−39] Because porosity regulation within composite cathodes critically influences ASSB electrochemical performance, the porosity of unimodal composite cathodes (UCCs) and bimodal composite cathodes (BCCs) was systematically evaluated.[32,40,41] To verify whether blending large polycrystalline NCWA with small single-crystalline NCM reduces porosity and improves packing density, tap-density measurements, He pycnometry, and scanning electron microscopy (SEM) were performed. The CAM fraction was fixed at 90 wt% in all composite cathodes to maximize energy density. For improved CAM/SSE interfacial contact, wet-milled $Li_{5.5}PS_{4.5}Cl_{1.5}$ (S-LPSCl1.5; D_{50} = 0.72 μm) was used as the SSE, and Super P was used as the CC, maintaining CAM:SSE:CC = 90:9.5:0.5 by weight (details are provided in the Supporting Information, Experimental Methods). UCCs were prepared using only NCWA or only NCM, denoted CAM10:0 and CAM0:10, respectively. BCCs were prepared by blending NCWA and NCM at 8:2, 7:3, and 6:4 weight ratios, denoted CAM8:2, CAM7:3, and CAM6:4. Tap densities for CAM-only blends and complete composite mixtures (including SSE and CC) are summarized in Table S1. As expected, bimodal CAM powders show increased tap density and the corresponding composite cathodes also exhibit enhanced packing density, although the improvement is smaller than in the CAM-only mixtures because SSE particles convert a unimodal system into a bimodal one and a bimodal system into a trimodal configuration. Cross-sectional SEM images of cathodes cold-pressed at 300 MPa are shown in Figure 1a, where pores are highlighted in red. Elemental distribution maps obtained via energy-dispersive X-ray spectroscopy (EDS) and the corresponding unmarked SEM images are provided in Figure S1. Even with SSE and CC present, NCM is homogeneously distributed among NCWA particles, and the ductile SSE fills interstitial voids between NCWA and NCM particles, producing a denser electrode structure. Figure 1b further visualizes the pore size and distribution. BCCs exhibit markedly reduced total pore area compared with

https://doi.org/10.1021/acsenergylett.5c03923
ACS Energy Lett. 2026, 11, 2103−2114

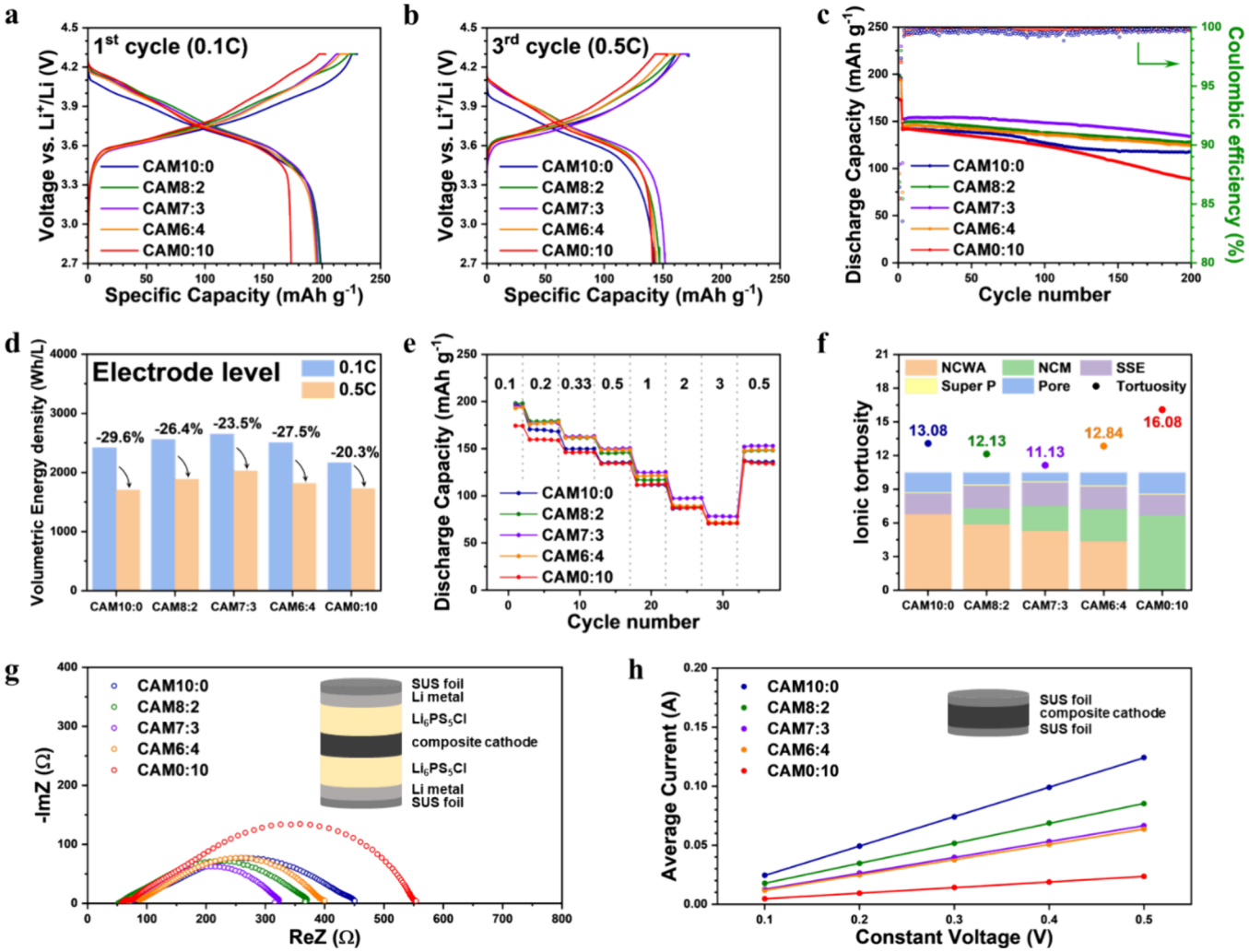

Figure 2. Electrochemical characterization of composite cathodes. (a) First charge/discharge profiles of ASSB cells at 0.1 C. (b) First charge/discharge profiles at 0.5 C. (c) Cycling stability over 200 galvanostatic cycles at 0.5 C. (d) Volumetric energy densities of each composite cathode at 0.1 and 0.5 C, and the percentage decrease in energy density with increasing C-rate (volumetric energy density refers only to the composite cathode). (e) Rate performance of ASSBs at various C-rates from 0.1 to 3 C. The numbers at the top indicate the C-rate applied at each rate step. (f) Volume fractions of materials and pores, and tortuosity values derived from these volume fractions. Colors in the columns represent the material volume fractions for each composite cathode, and the overlaid dots indicate the corresponding ionic tortuosity factors. (g) Nyquist plots of AC impedance for electron-blocking cells fabricated with each composite cathode; the cell configuration was [SUS foil | Li metal | Li_6PS_5Cl | composite cathode | Li_6PS_5Cl | Li metal | SUS foil], with a measurement frequency range of 5 MHz−1 mHz. (h) I−V plot derived from chronoamperometry curves of DC impedance for ion-blocking cells fabricated with each composite cathode; the cell configuration was [SUS foil | composite cathode | SUS foil], with measurement voltages ranging from 0.1 to 0.5 V in 0.1 V increments, each step maintained for 600 s. In (g) and (h), the symmetric cell configurations used to measure the effective ionic and electronic conductivities are shown.

UCCs. Although CAM10:0 and CAM0:10 show similar total pore areas, CAM10:0 contains a few large pores whereas CAM0:10 contains many small pores, indicating that CAM particle size directly influences the morphology and distribution of pores. Consequently, CAM10:0 likely possesses lower tortuosity than CAM0:10, a hypothesis that will be substantiated through subsequent electrochemical analyses. To provide a quantitative comparison beyond visual inspection, porosity was calculated using image analysis software (ImageJ; National Institutes of Health, USA) by determining the ratio of the red-marked pore area to the total area, as presented in Table S1.[22] The porosity of CAM10:0 and CAM0:10 were 16.8% and 18.0%, respectively, whereas those of CAM8:2, CAM7:3, and CAM6:4 were 10.2%, 7.6%, and 10.9%, respectively. These results confirm that BCCs achieve approximately 35%−58% lower porosity than UCCs, with minor variations depending on the NCWA-to-NCM ratio. For cross-validation and to complement the two-dimensional image analysis, He pycnometry measurements were performed, and the results are summarized in Table S1.[25] Consistent with the SEM-based analysis, BCCs exhibited lower porosity (8%−11%) compared with UCCs (11%−13%), with CAM7:3 demonstrating the lowest porosity among all samples. Photographs of the composite cathode pellets used for He pycnometry are shown in Figure S2. Each pellet was prepared by pressing approximately 1 g of composite cathode powder under identical conditions to ensure consistency across all samples.

To assess the electrochemical performance of each composite cathode, galvanostatic cycling tests were conducted within the voltage range of 2.7−4.3 V versus Li^+/Li. The protocol consisted of two formation cycles at 0.1 C, followed

https://doi.org/10.1021/acsenergylett.5c03923
ACS Energy Lett. 2026, 11, 2103−2114

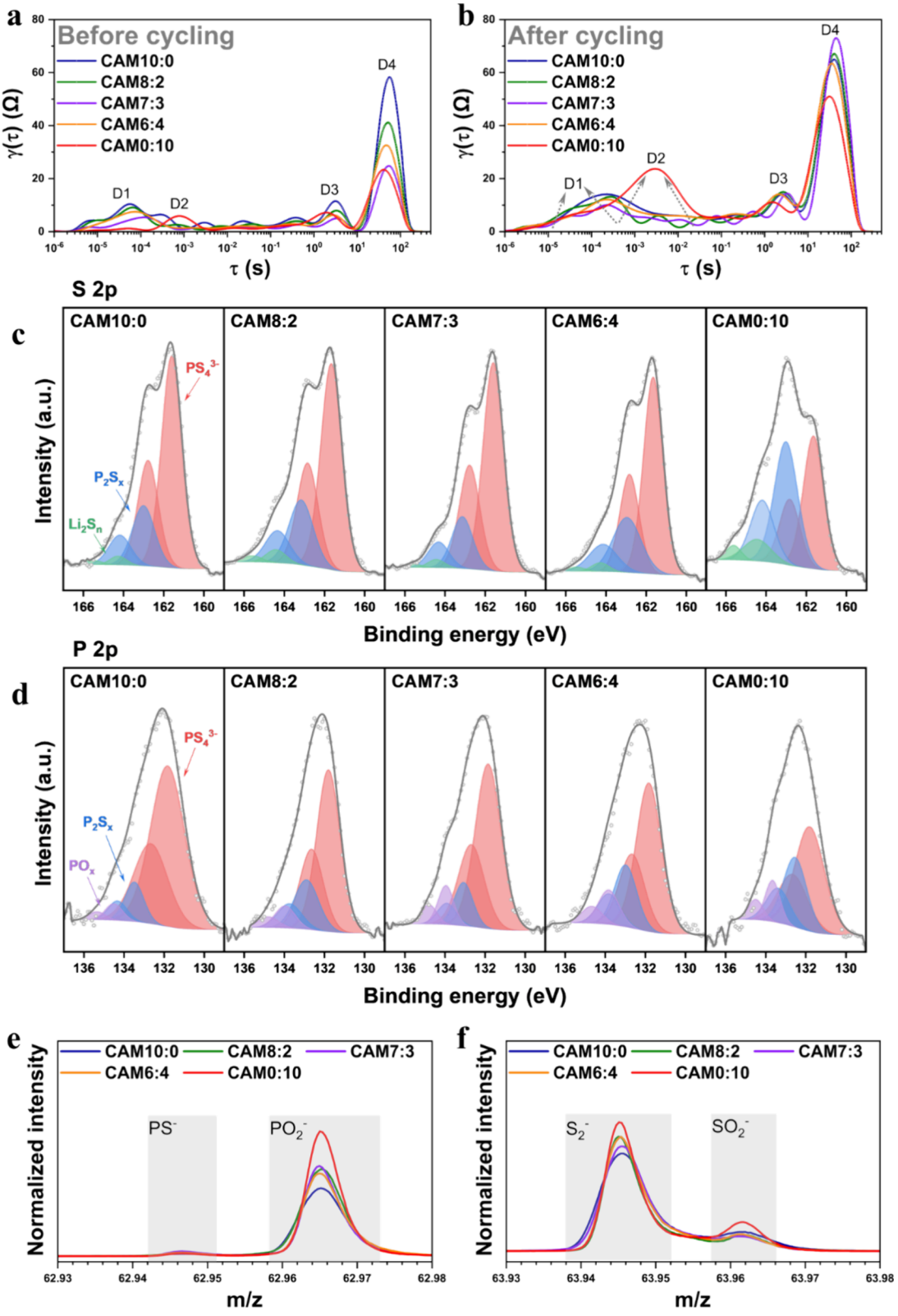

Figure 3. Electrochemical impedance spectroscopy (EIS) analysis and surface characterization of the composite cathodes. Distribution of relaxation time (DRT) curves obtained (a) before and (b) after galvanostatic cycling, with peaks D1−D4 assigned to distinct kinetic processes. X-ray photoelectron spectra of (c) S 2p and (d) P 2p acquired after galvanostatic cycling. Time-of-flight secondary ion mass spectrometry (ToF-SIMS) spectra of negatively charged interfacial fragments: (e) PS_4^{3-}-related fragment PS^- (m/z = 62.9458) and phosphate-related fragment PO_2^- (m/z = 62.9636); (f) polysulfide-related fragment S_2^- (m/z = 63.9441) and sulfite/sulfate-related fragment SO_2^- (m/z = 63.9619).

by continuous cycling at 0.5 C from the third cycle onward. The first-cycle voltage profile is shown in Figure 2a and the initial performance metrics are summarized in Table S2. Since five types of composite cathodes were compared, detailed

https://doi.org/10.1021/acsenergylett.5c03923
ACS Energy Lett. 2026, 11, 2103−2114

quantitative data are presented in the Supporting Information to enhance readability, while the main text focuses on qualitative interpretation. At 0.1 C, CAM10:0 exhibited higher discharge capacity and Coulombic efficiency than CAM0:10, mainly due to its higher Ni content and larger D_{50}. BCCs delivered higher Coulombic efficiencies than UCCs, but their discharge capacities decreased slightly with increasing NCM content and were generally lower than CAM10:0. At 0.5 C (Figure 2b and Table S3), the trend changed: CAM10:0 and CAM0:10 showed comparable discharge capacities, and CAM7:3 achieved the highest capacity among all compositions. CAM8:2 and CAM6:4 also outperformed both UCCs. These results suggest that at low current (0.1 C) the Ni content of the CAM predominantly governs discharge capacity, whereas at higher rates (0.5 C) electrode-level factors such as porosity, packing density, and effective ionic conductivity become dominant. Nonetheless, intrinsic CAM characteristics remain influential. In particular, CAM0:10 exhibited a higher capacity retention from 0.1 to 0.5 C than BCCs, consistent with the superior rate capability expected from the high specific surface area and short diffusion length of NCM. However, this large surface area is detrimental to long-term stability. As shown in Figure 2c, CAM0:10 exhibited the most severe capacity fading over 200 cycles, which was amplified by the high CAM loading (90 wt%). In contrast, CAM10:0 showed relatively stable cycling because its lower surface area suppresses parasitic CAM-SSE reactions, and the rod-like NCWA primary particles provide improved mechanical strength compared with conventional polycrystalline CAMs (Figure S3).[29,35,36] All BCCs exhibited significantly enhanced cycling stability relative to UCCs. The improvement in long-term performance, despite an increase in surface area compared with CAM10:0, suggests that the primary factors contributing to capacity degradation extend beyond secondary particle fracture and interfacial reactions. The results imply that optimized porosity control in the BCCs plays a decisive role in mitigating mechanical and electrochemical degradation, thereby sustaining stable cycling. Figure 2d and Table S3 summarize volumetric energy densities calculated using packing densities (Table S1) and discharge capacities at 0.1 and 0.5 C. BCCs achieve higher volumetric energy density than UCCs due to increased packing density and enhanced discharge capacities. To accurately evaluate rate-dependent behavior, rate performance tests were conducted (Figure 2e), and discharge capacities at each current rate are summarized in Table S4. At 0.1 C, CAM10:0 delivered the highest capacity, but its capacity declined rapidly with increasing C-rate and became the lowest at 0.5 C. In contrast, CAM0:10 showed the lowest capacity at 0.1 C, yet reached a discharge capacity comparable to CAM10:0 at 0.5 C, indicating excellent rate capability despite low initial capacity. Although the BCCs exhibited slightly lower capacities than CAM10:0 at 0.1 C, they showed markedly improved rate performance over the UCCs at 0.33−1 C. Notably, CAM7:3, with the densest electrode structure, maintained outstanding capacities at 2−3 C, outperforming CAM8:2 and CAM6:4. Therefore, beyond simply mixing NCWA and NCM, determining the optimal ratio is essential for improving both cycling stability and rate capability. Moreover, combining NCM—which provides superior rate performance but limited cycling stability—with NCWA, which exhibits contrasting intrinsic properties, represents a strategy that leverages the complementary advantages of both materials. To elucidate the electrode characteristics of UCCs and BCCs, effective ionic and electronic conductivity measurements were conducted, with results shown in Figure 2g and h and summarized in Table S5.[23] The BCCs facilitated Li^+ transport through reduced porosity, resulting in higher effective ionic conductivity than that of the UCCs.[42] Notably, although CAM10:0 and CAM0:10 have similar porosity, their effective ionic conductivities differ significantly. This discrepancy arises because, as seen in Figure 1, even when total pore volumes are comparable, the actual pore size and distribution significantly influence ionic transport, with CAM10:0 exhibiting much lower tortuosity than CAM0:10. In practice, when tortuosity values are calculated using the bulk ionic conductivity of the SSE and the SSE volume fraction within the electrode—taking into account the constituent materials and pores—a clear difference emerges between CAM10:0 and CAM0:10. This distinction can lead to meaningful variations in electrochemical performance, even under similar porosity conditions (Figure 2f and Table S6). Furthermore, the BCCs exhibited lower tortuosity overall, as reduced porosity promotes more efficient Li^+ transport and higher effective ionic conductivity.[43] In contrast, the effective electronic conductivity showed little correlation with porosity (Figure 2h).[42] It increased with the volume fraction of large NCWA particles, likely because larger CAM particles reduce interfacial transport resistance between CAM and CC, thereby enhancing electronic percolation and effective conductivity.[42] The chronoamperometry curves used for DC polarization fitting in Figure 2h are shown in Figure S4. Considering electrode structure and porosity alongside the effective ionic and electronic conductivities, CAM8:2 and CAM6:4 exhibited comparable overall performance: CAM8:2 benefited from slightly higher effective ionic conductivity, while CAM6:4 showed an advantage from a higher NCM content favoring rate performance. CAM7:3, where these two effects are well balanced, demonstrated the best cycling stability and rate performance among all tested compositions.

To identify differences in the cycling stability of each composite cathode, electrochemical impedance spectroscopy (EIS) was performed before and after galvanostatic cycling. To minimize variations associated with the state of charge (SOC), EIS was measured after the first charge at 0.5 C following the formation cycles ("before cycling", Figure S5). Since cathode-side decomposition typically dominates impedance increase and LTO is electrochemically stable with negligible volume change, the anode is expected to have a limited influence on the high- and mid-frequency semicircle.[44,45] After cycling, the impedance increase in UCCs was larger than in BCCs, and CAM0:10 showed the most pronounced rise. Although EIS is a reliable technique, it is difficult to distinguish the individual components contributing to the resistance increase; therefore, distribution of relaxation time (DRT) analysis was applied (Figures 3a and 3b). Each kinetic process has a unique time constant (τ) and forms a distinct peak, but adjacent processes may overlap, producing merged peaks that are difficult to separate.[46,47] For clarity, four peaks were assigned: D1 (10^{-6}–10^{-4} s) for accumulated mechanical degradation in the composite cathode (CAM−SSE and SSE−SSE contact loss), D2 (10^{-4}–10^{-1} s) for Li^+ transport across interfaces and charge-transfer resistance within the composite cathode, D3 (10^{-1}–10^{1} s) for interfacial resistance at the anode, and D4 (10^{1}–10^{2} s) for solid-state Li^+ diffusion.[46,48−50] Since identical composite anodes were used, D3 showed similar magnitudes among cells and differed mainly between pre- and post-cycling states. For D4, given the same anode configuration, variations

https://doi.org/10.1021/acsenergylett.5c03923
ACS Energy Lett. 2026, 11, 2103−2114

between composite cathodes were expected due to differences in Li^+ transport between NCWA and NCM. However, no clear trend was observed before or after cycling. This can be attributed to the fact that, as shown in Figure S6, the DRT fitting curve closely matches the EIS data in the high- and mid-frequency regions but deviates in the low-frequency region.[48,51] Accurate evaluation of diffusion-related processes therefore requires EIS data extending into the ultralow-frequency range (<0.01 Hz). In contrast, D1 and D2 exhibited clear and distinguishable changes, indicating that the dominant degradation mechanisms differed among the composite cathodes. D1 was largest for CAM10:0, whereas CAM0:10 and CAM7:3 exhibited the least degradation. Previous studies have shown that single-crystalline CAMs exhibit smaller pressure fluctuations than polycrystalline CAMs, consistent with the interpretation that CAM0:10 accumulates less mechanical damage.[52−56] Importantly, CAM7:3 showed the D1 peak comparable to CAM0:10 despite containing a substantial NCWA fraction, demonstrating that the bimodal structure effectively mitigates mechanical degradation. CAM8:2 and CAM6:4, which have higher porosity than CAM7:3, showed larger D1 peaks, emphasizing the key role of porosity in mechanical stability. Nevertheless, further investigation is required to clarify how the controlled porosity enabled by the bimodal structure mitigates mechanical degradation, and this mechanism is discussed in detail in Figures 4 and 5. The D2 peak reflects two overlapping effects. First, CAM0:10 exhibited a notably high D2 peak, attributed to its large specific surface area, which promotes extensive CAM−SSE interfacial side reactions. Second, in the BCCs, reduced porosity enhanced effective ionic conductivity and minimized charge-transfer resistance, resulting in smaller D2 peaks compared with CAM10:0. Therefore, in the BCCs, the negative effects of an increased interfacial area—caused by NCM incorporation—were offset by the benefits of lower porosity and improved ionic transport. To verify the influence of surface side reactions related to CAM ratio, X-ray photoelectron spectroscopy (XPS) analysis was performed, and the results are shown in Figure 3c,d and Figure S7. In the S 2p spectra, the most intense peak at approximately 161.6 eV was assigned to the PS_4^{3-} unit of the argyrodite SSE structure,[57−59] and its intensity decreased from CAM10:0 to CAM0:10, consistent with its larger interfacial reaction area.[16] After cycling, the P_2S_x (163.0 eV) and Li_2S_n (164.4 eV) peaks became more pronounced,[60−65] and CAM0:10 showed that approximately 60% of the total signal area consisted of these signals, indicating that severe decomposition reactions occurred as a result of the high specific surface area of NCM. In the P 2p spectra, CAM0:10 exhibited large signal areas corresponding to P_2S_x (133.0 eV) and oxidized phosphorus species such as PO_x (134.0 eV), in clear contrast to the other composite cathodes.[59,61,62,64,66−68] Since clear inferences could not be made when comparing samples other than CAM0:10, semiquantitative ToF-SIMS analysis was performed, and the results are presented in Figure 3e and f. In the secondary-ion mass spectrum (m/z 62.93−62.98), the PS^- signal (m/z 62.9458) decreased after cycling for all composite cathodes, whereas, consistent with the XPS analysis, CAM0:10 exhibited the highest PO_2^- intensity (m/z 62.9636), confirming extensive phosphate formation.[64,69−71] In the m/z 63.93−63.98 range, CAM0:10 also showed the highest S_2^- (m/z 63.9441) and SO_2^- (m/z 63.9619) signals, indicating more extensive formation of sulfite- and sulfate-related side-reaction

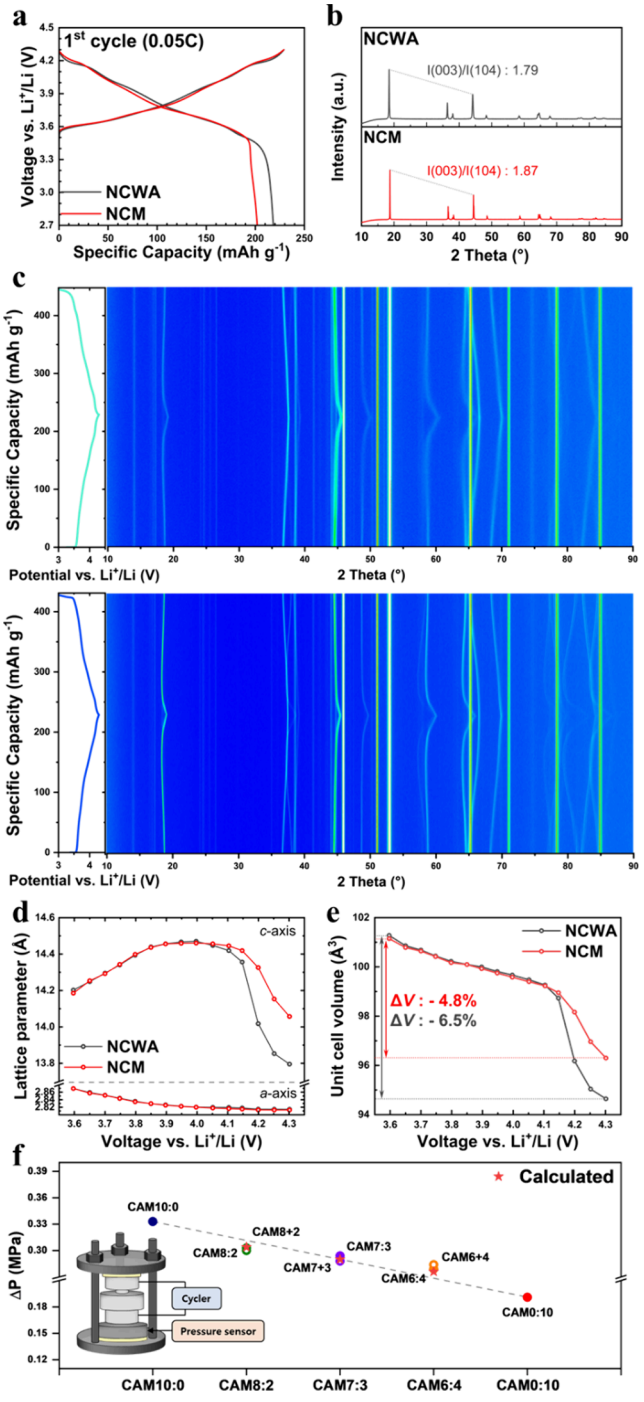

Figure 4. X-ray diffraction (XRD) analysis of CAMs and mechanical characterization of composite cathodes. (a) First charge/discharge profiles obtained during operando XRD of a LIB. (b) Powder XRD patterns of NCWA and NCM. (c) Contour plots of operando XRD patterns during the first cycle (right) with corresponding charge/discharge curves (left). The upper plots correspond to NCWA, and the lower to NCM. Peaks that remain stationary throughout cycling—appearing near $2\theta \approx 46°$, 51°, 53°, 71°, and 85°—originate from the Be window of the operando XRD cell kit (PDF #01-072-2381), while the additional peaks near 65° and 78° arise from the Al current collector (PDF #00-004-0787). (d) Variations in the *a*- and *c*-axis lattice parameters and (e) unit-cell volume with respect to cell voltage for NCWA and NCM. (f) Electrochemical pressiometry results for each composite cathode, showing the average pressure change measured during cycling at 0.5 C.

https://doi.org/10.1021/acsenergylett.5c03923
ACS Energy Lett. 2026, 11, 2103−2114

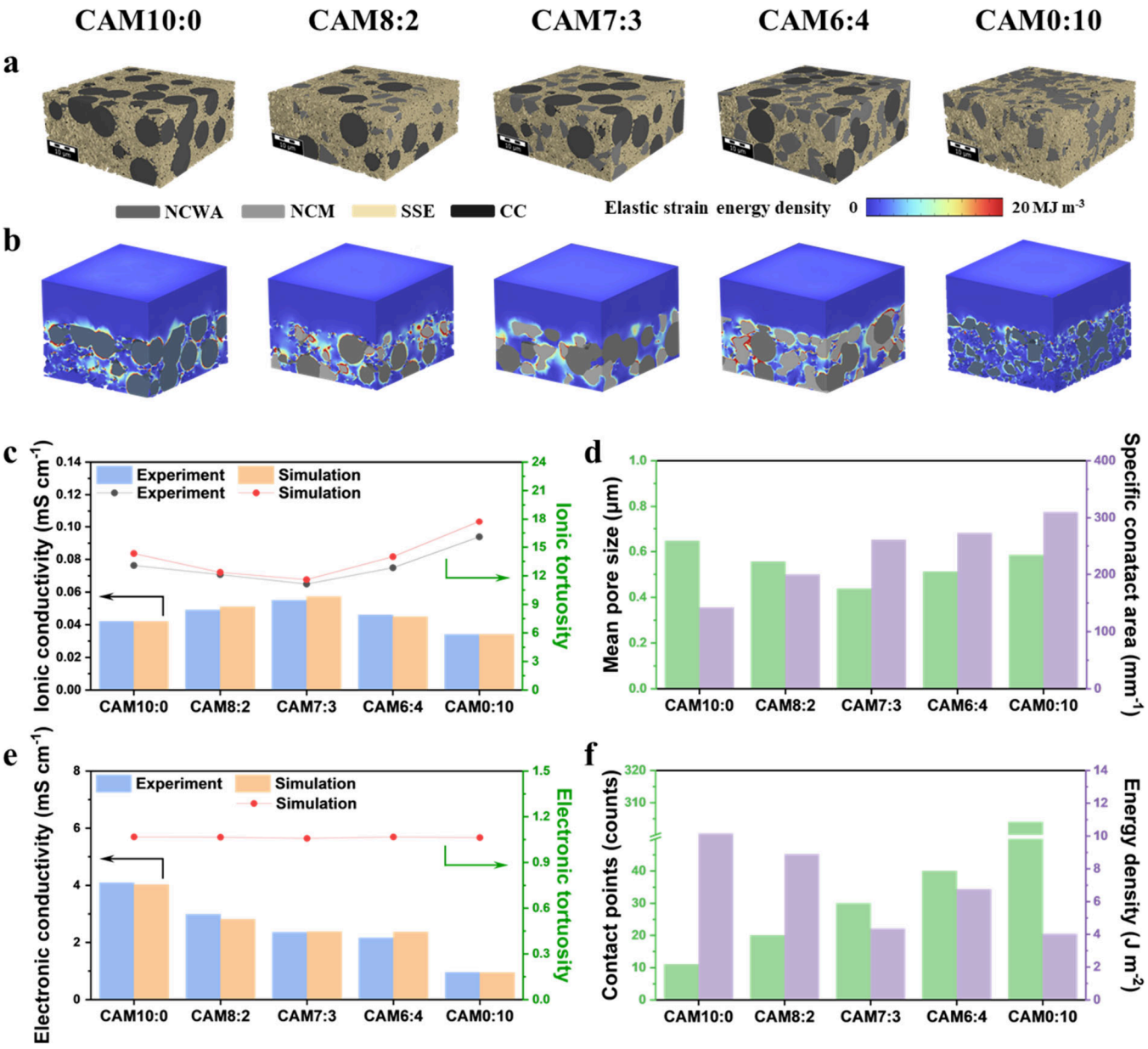

Figure 5. Cross-sectional SEM images from Figure 1 were utilized to reconstruct three-dimensional electrode structures (40 × 40 × thickness μm^3), as shown in Figure 5a. The thickness of each reconstructed model was determined from the tap density values listed in Table S1 to accurately reflect experimental variations in packing density and porosity. To more accurately model mechanical degradation resulting from CAM volume contraction, multiphysics simulations incorporated the experimentally obtained unit-cell volume change data shown in Figure 4e. (a) Three-dimensional reconstructed structures for each composite cathode as a function of CAM fraction. Colors denote materials as follows: gray, NCM; dark gray, NCWA; dark yellow, SSE; black, CC. (b) Elastic strain energy density in the composite cathodes during charging to 4.3 V (Li^+/Li), simulated by accounting for CAM contraction and porosity. (c) Experimental and simulated effective ionic conductivity and ionic tortuosity for each composite cathode. The bars represent ionic conductivity, and the circles represent ionic tortuosity. (d) Simulated mean pore size and simulated specific contact area of CAM−SSE for each composite cathode. The green bars represent the mean pore size, whereas the purple bars represent the specific contact area. (e) Experimental and simulated effective electronic conductivity, and electronic tortuosity derived from simulations. The bars represent electronic conductivity, and the circles represent electronic tortuosity. (f) Simulated CAM−CAM interparticle contact points and elastic strain energy density in each composite cathode. The green bars represent CAM−CAM particle contact points, whereas the purple bars represent elastic strain energy density.

products. Although XPS could not clearly distinguish differences between the BCCs and CAM10:0, the ToF-SIMS results suggest that the overall extent of interfacial side reactions was slightly higher in the BCCs. However, unlike PO_2^- and S_2^-, which exhibited consistent trends, CAM10:0 displayed higher SO_2^- intensity than the BCCs. This likely reflects variations in preferred reaction pathways influenced by differences in effective electronic conductivity and intermediate formation.[64,69,72] As similar inconsistencies have been reported previously, further investigation of sulfite and sulfate species is warranted. Overall, while CAM0:10 experienced the most extensive interfacial reactions, it is likely that BCCs also underwent interfacial side reactions at a larger number of localized sites than CAM10:0. Nevertheless, these reactions did not directly correlate with the overall electrochemical performance of the ASSBs, indicating that although interfacial

https://doi.org/10.1021/acsenergylett.5c03923
ACS Energy Lett. 2026, 11, 2103−2114

side reactions are critical, they are not the sole determinant of degradation behavior in composite cathodes.

In composite cathodes of ASSBs, cumulative internal stress generated by CAM volume changes affects the electrode microstructure, promotes mechanical degradation, and can ultimately lead to cell failure. Since NCWA and NCM differ in Ni content and microstructure, operando X-ray diffraction (XRD) was performed for both CAMs to quantify unit-cell volume changes during charge and discharge. Figure 4a presents the half-cell voltage profiles obtained during operando XRD. Owing to its higher Ni content, NCWA delivered a higher discharge capacity (218.3 mAh g^{-1}) than NCM (201.9 mAh g^{-1}). Consistent with the ASSB results, the smaller NCM particles with higher specific surface area showed a lower initial Coulombic efficiency (88.1%) than NCWA (95.3%). Figure 4b shows powder XRD patterns. The intensity ratios of the (003) to (104) peaks are 1.79 for NCWA and 1.87 for NCM, confirming well-developed hexagonal layered structures with minimal Li/Ni cation mixing.[73] The contour plots in Figure 4c illustrate the evolution of major diffraction peaks, including (003), (101), and (104). The upper contour plots correspond to NCWA, and the lower to NCM, with the associated voltage profiles shown on the left. The lattice parameters, space group, atomic coordinates, and occupancies used in the Rietveld refinement of the operando XRD data are listed in Table S7, and the Rietveld refinement results for each CAM are shown in Figure S8. The variations in lattice parameters as a function of voltage are presented in Figure 4d. Both CAMs exhibit characteristic behavior typical of high-Ni layered oxides. The *a*-axis contracts by 2.0% for both NCWA and NCM, while the *c*-axis initially expands gradually and then contracts abruptly—by 4.6% and 2.8%, respectively—around 4.15−4.2 V, corresponding to the H2−H3 phase transition. As shown in Figure 4e, the higher Ni content in NCWA results in a larger total unit-cell volume change (−6.5%) than that of NCM (−4.8%).[74,75] Subsequently, operando electrochemical pressiometry was conducted to evaluate internal stress variations within the composite cathodes during cycling in ASSBs.[34,76] The operando electrochemical pressiometry curves for each composite cathode are presented in Figure S9, and the corresponding stress change results are shown in Figure 4f. To correlate these results with the long-term galvanostatic cycling behavior, internal stress evolution was measured after two initial cycles at 0.1 C, followed by continuous cycling at 0.5 C. For the UCCs, CAM10:0 exhibited an internal stress change of 0.33 MPa, whereas CAM0:10 showed a smaller change of 0.19 MPa. Despite using NCWA with an optimized primary particle morphology and enhanced preferred orientation, CAM10:0 still experienced larger internal stress changes than CAM0:10. Although variations in Ni content could contribute to this difference, it should be noted that the operando pressiometry tests were conducted at 0.5 C, where the ASSBs delivered discharge capacities of only 140−150 mAh g^{-1}—significantly lower than the capacities obtained at 0.05 C in the operando XRD experiments. Hence, the CAMs were not fully lithiated and delithiated during measurement, and the actual volume changes would have been smaller. Therefore, the larger internal stress variation observed for the large polycrystalline CAM is attributed primarily to its intrinsic material characteristics. Subsequently, internal stress changes were measured for the BCCs using the same protocol, and detailed values are summarized in Table S8. The measured stress changes were 0.303, 0.294, and 0.279 MPa for CAM8:2, CAM7:3, and CAM6:4, respectively. These values closely matched those estimated by weighting the individual stress changes of CAM10:0 and CAM0:10 according to their respective mass ratios. This finding indicates that the incorporation of small NCM particles between large NCWA particles, and the associated reduction in porosity, does not directly diminish the overall pressure variations. Instead, the magnitude of internal stress change is governed primarily by the relative CAM mass fractions within the electrode. Moreover, the comparable stress evolutions observed among the BCCs suggest that their enhanced mechanical stability arises not from a reduction in internal stress generation but from an increased resistance to mechanical deformation. To further verify that internal stress change is determined by the CAM fraction rather than the macrostructural configuration, operando electrochemical pressiometry was repeated using modified composite cathodes. In these tests, premixed CAM10:0 and CAM0:10 composites were sequentially loaded into the SSE pellets at mass ratios of 8:2, 7:3, and 6:4, producing samples designated as CAM8+2, CAM7+3, and CAM6+4, respectively. The resulting pressure profiles were nearly identical to those of the original CAM8:2, CAM7:3, and CAM6:4 cathodes. Taken together, these results confirm that, despite notable differences in the spatial distribution of NCWA and NCM particles and in electrode porosity, the overall internal pressure variations remain essentially unchanged. Therefore, the enhanced mechanical stability and reduced degradation observed in BCCs originate not from pressure relief but from the strengthened mechanical integrity of the composite architecture, which resists stress-induced damage and contributes to improved cycling stability in ASSBs.

Digital-twin simulations were performed to comprehensively evaluate the effects of CAM expansion and contraction, as well as the influence of electrode structural parameters, including porosity differences. Reconstructed three-dimensional electrode structures are shown in Figure 5a. Model validity was verified by comparing the simulated ionic and electronic conductivities with the corresponding experimental results, and the validated models were then used to perform multiphysics simulations accounting for CAM contraction and expansion. Detailed procedures for electrode reconstruction and simulation conditions are described in the Supporting Information, Experimental Methods. The experimental and simulated effective ionic conductivities for each composite cathode are presented in Figure 5c and Table S9. Consistent with experimental observations, BCCs exhibited higher effective ionic conductivity than UCCs, with values following the order CAM6:4 < CAM8:2 < CAM7:3. The average deviation between simulated and experimental results was 1.98%, confirming that the 3D models accurately replicate the actual electrochemical behavior. The simulated ionic tortuosity also showed the same trend as that derived from experiments. To further elucidate the influence of CAM ratio and electrode structure on effective ionic conductivity and ionic tortuosity, additional multiphysics simulations were conducted using the reconstructed 3D electrodes. Figure 5d presents the mean pore size and the specific contact area between the CAM and SSE for each composite cathode, with detailed values provided in Table S10. As also observed in Figure 1, CAM0:10 exhibited a smaller mean pore size than CAM10:0, and CAM6:4 showed a smaller mean than CAM8:2. Considering the overall porosity, increasing the NCM fraction reduced mean pore size but increased the total number of pores, which lengthened Li^+

https://doi.org/10.1021/acsenergylett.5c03923
ACS Energy Lett. 2026, 11, 2103−2114

conduction pathways, increased tortuosity, and reduced effective ionic conductivity. Despite having the smallest mean pore size, CAM7:3 maintained the highest effective ionic conductivity because its exceptionally low porosity provides the shortest Li^+ transport pathways. Thus, while total porosity is dominant, ionic transport is governed by the combined effects of pore size and pore number. Additionally, the specific CAM−SSE interfacial area increased consistently with increasing NCM fraction. This observation aligns with the results in Figures 2 and 3, indicating that higher NCM content provides more potential sites for interfacial side reactions during electrochemical cycling. Figure 5e and Table S11 present the experimental effective electronic conductivity, the simulated effective electronic conductivity, and the simulated electronic tortuosity. The 3.66% discrepancy between simulated and experimental values confirms that the reconstructed models accurately reproduce the actual composite electrode structure. Because the composite cathodes contain 90 wt% CAM, a percolating electronic network is already formed, and CAM−CAM interfacial resistance mainly governs electronic transport, leading to only minor variations in electronic tortuosity. Figure 5f and Table S12 show the number of CAM−CAM interparticle contacts in the 3D reconstructed electrodes. Contact points increased with NCM fraction, with CAM0:10 exhibiting the highest count. Since electron transport between CAM particles is more resistive than conduction within CAM itself, these results indicate that, at similar tortuosity, the particle size of CAM critically influences the effective electronic conductivity of the composite cathode.[77,78] Figure 5b shows the simulated elastic strain energy density distribution in the SSE caused by CAM contraction during charging to 4.3 V versus Li^+/Li. Regions of high stress concentration are depicted in red. Because smaller NCM particles undergo less contraction than larger NCWA particles, the local elastic strain energy density at the SSE interface is relatively lower for NCM-based cathodes. On a larger scale, examining the CAM−SSE interfaces across the entire electrode reveals greater mechanical instability in CAM10:0 compared with CAM0:10 (Figure 5f, Table S12). This difference arises because a denser, more interconnected SSE framework formed under reduced porosity effectively buffers mechanical stress and distributes strain from CAM contraction, maintaining robust interfacial contact. Accordingly, BCCs with efficient packing show higher mechanical stability than CAM10:0. Among the BCCs, CAM7:3—with its most densely packed electrode structure—exhibited elastic strain energy density comparable to CAM0:10 and delivered the best electrochemical performance, identifying it as the optimal BCC ratio.

This study demonstrates that electrode-level engineering using BCCs provides an effective strategy to overcome the intrinsic limitations of individual CAMs in ASSBs. The UCCs exhibit inherent trade-offs: NCWA-based UCCs suffer from limited rate performance and reduced mechanical stability, whereas NCM-based UCCs exhibit intensified interfacial side reactions and lower volumetric energy density. By filling voids between NCWA with NCM, BCCs lower porosity, raise effective ionic conductivity, and reduce ionic tortuosity. The optimized CAM7:3 delivered the highest capacity at 0.5 C, sustained strong performance at 2−3 C, and showed the best electrochemical stability over 200 cycles. DRT analysis of EIS, together with post-mortem XPS and ToF-SIMS, indicated that interfacial reactions contribute but do not solely govern degradation. Operando XRD and operando electrochemical pressiometry provided key mechanistic insights into the relationship between electrochemical behavior and mechanical degradation. Independent of the intrinsic stress variations in UCCs, internal stress variations in BCCs were governed mainly by the mass-weighted contributions of each CAM rather than by the electrode's structural arrangement or porosity. Digital-twin simulations confirmed reduced tortuosity and more uniform deformation, minimizing CAM−SSE stress concentrations and mechanical degradation. These findings underscore the critical role of electrode-level design in unlocking the full potential of ASSBs and provide practical guidance for developing next-generation composite cathodes with tailored macrostructures and superior performance.

■ ASSOCIATED CONTENT

Supporting Information

The Supporting Information is available free of charge at https://pubs.acs.org/doi/10.1021/acsenergylett.5c03923.

Experimental methods, Cross-sectional SEM image of composite cathode with corresponding EDS mapping, Cross-sectional SEM images of the NCWA, Tap density of composite cathode, Composite cathode pellet used for He pycnometry measurements, 1st cycle electrochemical performance for each composite cathode, Cycling stability performance data for each composite cathode, Rate performance for each composite cathode, Effective conductivity for each composite cathode, Ionic tortuosity of each composite cathode and the volume of each material within the composite cathode, Chronoamperometry curves for each composite cathode, Nyquist plots from EIS with the corresponding fitting lines, XPS spectra measured prior to galvanostatic cycling, Rietveld refinement of XRD data of NCWA and NCM, Operando electrochemical pressiometry results for each composite cathode, Simulated effective conductivity and tortuosity, Simulated mean pore size and the specific contact area between CAM and SSE, Material parameters for each component, Symbols, values, units, and descriptions for each parameter, EIS data for SSE, PSA data for CAM and SSE, Young's modulus of layered oxides with lithium concentration (PDF)

■ AUTHOR INFORMATION

Corresponding Authors

Hun-Gi Jung − *Energy Storage Research Center, Sustainable Energy Research Division, Korea Institute of Science and Technology, Seoul 02792, Republic of Korea; KIST-SKKU Carbon-Neutral Research Center, Sungkyunkwan University, Suwon 16419, Republic of Korea; Department of Energy Science, Sungkyunkwan University, Suwon 16419, Republic of Korea; Division of Energy and Environment Technology, KIST School, Korea University of Science and Technology, Seoul 02792, Republic of Korea;* orcid.org/0000-0002-2162-2680; Phone: +82 2 958 5240; Email: hungi@kist.re.kr; Fax: +82 2 958 5229

Jong-Won Lee − *Division of Materials Science and Engineering, Hanyang University, Seoul 04763, Republic of Korea; Department of Battery Engineering, Hanyang University, Seoul 04763, Republic of Korea;* orcid.org/0000-0002-8713-7143; Email: jongwonlee@hanyang.ac.kr

https://doi.org/10.1021/acsenergylett.5c03923
ACS Energy Lett. 2026, 11, 2103−2114

Sang-Young Lee − *Department of Chemical and Biomolecular Engineering, Yonsei University, Seoul 03722, Republic of Korea;* orcid.org/0000-0001-7153-0517; Email: syleek@yonsei.ac.kr

Authors

Hyeonseong Oh − *Energy Storage Research Center, Sustainable Energy Research Division, Korea Institute of Science and Technology, Seoul 02792, Republic of Korea; Department of Chemical and Biomolecular Engineering, Yonsei University, Seoul 03722, Republic of Korea*

Uigyeong Jeong − *Energy Storage Research Center, Sustainable Energy Research Division, Korea Institute of Science and Technology, Seoul 02792, Republic of Korea; Division of Materials Science and Engineering, Hanyang University, Seoul 04763, Republic of Korea*

Junhyeok Choi − *Department of Battery Engineering, Yonsei University, Seoul 03722, Republic of Korea*

Jaejin Lim − *Department of Chemical and Biomolecular Engineering, Yonsei University, Seoul 03722, Republic of Korea*

Jun Tae Kim − *Energy Storage Research Center, Sustainable Energy Research Division, Korea Institute of Science and Technology, Seoul 02792, Republic of Korea*

Hyeon-Ji Shin − *Energy Storage Research Center, Sustainable Energy Research Division, Korea Institute of Science and Technology, Seoul 02792, Republic of Korea*

Jong-yeon Im − *Energy Storage Research Center, Sustainable Energy Research Division, Korea Institute of Science and Technology, Seoul 02792, Republic of Korea*

Hyun-Woo Gong − *Advanced Analysis and Data Center, Korea Institute of Science and Technology, Seoul 02792, Republic of Korea*

Jae-Pyoung Ahn − *Advanced Analysis and Data Center, Korea Institute of Science and Technology, Seoul 02792, Republic of Korea;* orcid.org/0000-0003-2657-7425

Yong Min Lee − *Department of Chemical and Biomolecular Engineering, Yonsei University, Seoul 03722, Republic of Korea; Department of Battery Engineering, Yonsei University, Seoul 03722, Republic of Korea;* orcid.org/0000-0003-2002-2218

Jongsoon Kim − *KIST-SKKU Carbon-Neutral Research Center, Sungkyunkwan University, Suwon 16419, Republic of Korea; Department of Energy Science, Sungkyunkwan University, Suwon 16419, Republic of Korea*

Junyoung Mun − *Energy Storage Research Center, Sustainable Energy Research Division, Korea Institute of Science and Technology, Seoul 02792, Republic of Korea; KIST-SKKU Carbon-Neutral Research Center, Sungkyunkwan University, Suwon 16419, Republic of Korea*

Kyung Yoon Chung − *Energy Storage Research Center, Sustainable Energy Research Division, Korea Institute of Science and Technology, Seoul 02792, Republic of Korea; Division of Energy and Environment Technology, KIST School, Korea University of Science and Technology, Seoul 02792, Republic of Korea;* orcid.org/0000-0002-1273-746X

Si Hyoung Oh − *Energy Storage Research Center, Sustainable Energy Research Division, Korea Institute of Science and Technology, Seoul 02792, Republic of Korea;* orcid.org/0000-0002-7063-9235

Complete contact information is available at: https://pubs.acs.org/10.1021/acsenergylett.5c03923

Author Contributions

[¶]H.O. and U.J. contributed equally to this work. H.O. conceptualized the study, designed the methodology, performed the investigation, and wrote the original draft. U.J. prepared samples, performed formal analysis, created visualizations, and wrote the original draft. J.T.K., H.-J.S., J.-Y.I., and H.-W.G. conducted characterization and validation. J.C. and J.L. performed formal analysis and developed visualizations. J.-P.A., Y.M.L., J.M., J.K., K.Y.C., and S.H.O. provided supervision. J.-W.L. and S.-Y.L. provided supervision and resources. H.-G.J. acquired funding, administered the project, and wrote, reviewed, and edited the manuscript.

Notes

The authors declare no competing financial interest.

■ ACKNOWLEDGMENTS

This work was supported by the Korea Institute of Science and Technology (KIST) Institutional Program (26E0322); the National Research Foundation of Korea (NRF) funded by the Ministry of Science and ICT (No. RS-2025-23523434); the Development Program of Core Industrial Technology funded by the Ministry of Trade, Industry and Energy of Korea (No. 20007045); and the National Research Council of Science and Technology (NST) grant of Korea (No. GTL24011-000).

■ REFERENCES

(1) Larcher, D.; Tarascon, J.-M. Towards greener and more sustainable batteries for electrical energy storage. *Nature Chem.* **2015**, *7* (1), 19−29.

(2) Kittner, N.; Lill, F.; Kammen, D. M. Energy storage deployment and innovation for the clean energy transition. *Nature Energy* **2017**, *2* (9), 1−6.

(3) Choi, J. W.; Aurbach, D. Promise and reality of post-lithium-ion batteries with high energy densities. *Nature Reviews Materials* **2016**, *1* (4), 16013.

(4) Wang, Q.; Ping, P.; Zhao, X.; Chu, G.; Sun, J.; Chen, C. Thermal runaway caused fire and explosion of lithium ion battery. *J. Power Sources* **2012**, *208*, 210−224.

(5) Eshetu, G. G.; Bertrand, J.-P.; Lecocq, A.; Grugeon, S.; Laruelle, S.; Armand, M.; Marlair, G. Fire behavior of carbonates-based electrolytes used in Li-ion rechargeable batteries with a focus on the role of the LiPF6 and LiFSI salts. *J. Power Sources* **2014**, *269*, 804−811.

(6) Gao, Z.; Sun, H.; Fu, L.; Ye, F.; Zhang, Y.; Luo, W.; Huang, Y. Promises, challenges, and recent progress of inorganic solid-state electrolytes for all-solid-state lithium batteries. *Advanced Materials* **2018**, *30* (17), 1705702.

(7) Xi, G.; Xiao, M.; Wang, S.; Han, D.; Li, Y.; Meng, Y. Polymer-based solid electrolytes: material selection, design, and application. *Adv. Funct. Mater.* **2021**, *31* (9), 2007598.

(8) Park, K.-H.; Kaup, K.; Assoud, A.; Zhang, Q.; Wu, X.; Nazar, L. F. High-voltage superionic halide solid electrolytes for all-solid-state Li-ion batteries. *ACS Energy Letters* **2020**, *5* (2), 533−539.

(9) Chen, S.; Xie, D.; Liu, G.; Mwizerwa, J. P.; Zhang, Q.; Zhao, Y.; Xu, X.; Yao, X. Sulfide solid electrolytes for all-solid-state lithium batteries: Structure, conductivity, stability and application. *Energy Storage Materials* **2018**, *14*, 58−74.

(10) Janek, J.; Zeier, W. G. A solid future for battery development. *Nature energy* **2016**, *1* (9), 16141.

(11) Kim, K. J.; Balaish, M.; Wadaguchi, M.; Kong, L.; Rupp, J. L. Solid-state Li-metal batteries: challenges and horizons of oxide and sulfide solid electrolytes and their interfaces. *Adv. Energy Mater.* **2021**, *11* (1), 2002689.

(12) Miura, A.; Rosero-Navarro, N. C.; Sakuda, A.; Tadanaga, K.; Phuc, N. H.; Matsuda, A.; Machida, N.; Hayashi, A.; Tatsumisago, M. Liquid-phase syntheses of sulfide electrolytes for all-solid-state lithium battery. *Nature Reviews Chemistry* **2019**, *3* (3), 189−198.
(13) Adeli, P.; Bazak, J. D.; Park, K. H.; Kochetkov, I.; Huq, A.; Goward, G. R.; Nazar, L. F. Boosting solid-state diffusivity and conductivity in lithium superionic argyrodites by halide substitution. *Angew. Chem., Int. Ed.* **2019**, *58* (26), 8681−8686.
(14) Wu, J.; Liu, S.; Han, F.; Yao, X.; Wang, C. Lithium/sulfide all-solid-state batteries using sulfide electrolytes. *Adv. Mater.* **2021**, *33* (6), 2000751.
(15) Wu, J.; Shen, L.; Zhang, Z.; Liu, G.; Wang, Z.; Zhou, D.; Wan, H.; Xu, X.; Yao, X. All-solid-state lithium batteries with sulfide electrolytes and oxide cathodes. *Electrochemical Energy Reviews* **2021**, *4* (1), 101−135.
(16) Kim, J. T.; Shin, H.-J.; Kim, A-Y.; Oh, H.; Kim, H.; Yu, S.; Kim, H.; Chung, K. Y.; Kim, J.; Sun, Y.-K.; Jung, H.-G. An argyrodite sulfide coated NCM cathode for improved interfacial contact in normal-pressure operational all-solid-state batteries. *Journal of Materials Chemistry A* **2023**, *11* (38), 20549−20558.
(17) Xiao, Y.; Wang, Y.; Bo, S.-H.; Kim, J. C.; Miara, L. J.; Ceder, G. Understanding interface stability in solid-state batteries. *Nature Reviews Materials* **2020**, *5* (2), 105−126.
(18) Zhang, F.; Guo, Y.; Zhang, L.; Jia, P.; Liu, X.; Qiu, P.; Zhang, H.; Huang, J. A review of the effect of external pressure on all-solid-state batteries. *Etransportation* **2023**, *15*, 100220.
(19) Hong, S.-B.; Lee, Y.-J.; Kim, H.; Go, M. C.; Kim, U.-H.; Sun, Y.-K.; Kim, D.-W. Redefining Polymer Binders: Enabling Ion Transport and Interfacial Stability in Sulfide-Based All-Solid-State Lithium Batteries. *Energy Storage Materials* **2025**, *83*, 104756.
(20) Lee, K.; Lee, J.; Choi, S.; Char, K.; Choi, J. W. Thiol-ene click reaction for fine polarity tuning of polymeric binders in solution-processed all-solid-state batteries. *ACS Energy Letters* **2019**, *4* (1), 94−101.
(21) Park, S. H.; Hwang, Y. Y.; Park, I.; Park, H. B.; Lee, Y. J. Mechano-chemical solution process for Li3PS4 solid electrolyte using dibromomethane for enhanced conductivity and cyclability in all-solid-state batteries. *Energy Storage Materials* **2023**, *63*, 102985.
(22) Jung, W. D.; Kim, J.-S.; Kim, Y. J.; Jeong, H.; Han, D.; Nam, K.-W.; Ahn, D.; Kwon, D.-H.; Jung, H.-G.; Lee, J.-H.; Kim, H. Annealing-Free Thioantimonate Argyrodites with High Li-Ion Conductivity and Low Elastic Modulus. *Adv. Funct. Mater.* **2023**, *33* (11), 2211185.
(23) Shin, H. J.; Kim, J. T.; Han, D.; Kim, H. S.; Chung, K. Y.; Mun, J.; Kim, J.; Nam, K. W.; Jung, H. G. 2D Graphene-Like Carbon Coated Solid Electrolyte for Reducing Inhomogeneous Reactions of All-Solid-State Batteries. *Adv. Energy Mater.* **2025**, *15* (1), 2403247.
(24) Sung, J.; Lee, H. G.; Jo, Y.-S.; Kim, D.-H.; Park, H.; Park, J.-H.; Kim, D.; Ha, Y.-C.; Baeg, K.-J.; Park, J.-W. Size-controlled wet-chemical synthesis of sulfide superionic conductors for high-performance all-solid-state batteries. *Energy Storage Materials* **2024**, *67*, 103253.
(25) Oh, H.; Kim, J. T.; Shin, H.-J.; Kim, A-Y.; Bak, C.; Kim, S.-O.; Chung, K. Y.; Mun, J.; Kim, J.; Lee, Y. M.; Lee, S.-Y.; Jung, H.-G. Stable performance for pouch-type all-solid-state batteries enabled by current collector with optimized primer layer. *Materials Science and Engineering: R: Reports* **2025**, *164*, 100970.
(26) Park, G.-T.; Ryu, H.-H.; Park, N.-Y.; Lee, S.-B.; Sun, Y.-K. Single-Crystal vs Polycrystalline Cathodes for Lithium-Ion Batteries. *Chem. Rev.* **2025**, *125*, 9930.
(27) Han, Y.; Jung, S. H.; Kwak, H.; Jun, S.; Kwak, H. H.; Lee, J. H.; Hong, S. T.; Jung, Y. S. Single-or poly-crystalline Ni-rich layered cathode, sulfide or halide solid electrolyte: which will be the winners for all-solid-state batteries? *Adv. Energy Mater.* **2021**, *11* (21), 2100126.
(28) Liu, H.; Wang, Y.; Chen, L.; Li, H.; Wu, F. High-Capacity, Long-Life Sulfide All-Solid-State Batteries with Single-Crystal Ni-Rich Layered Oxide Cathodes. *Adv. Funct. Mater.* **2024**, *34* (26), 2315701.
(29) Ryu, H.-H.; Sun, Y.-K. Nanorod Cathodes: A Solution for Polycrystalline Cathodes in Next-Generation Lithium Batteries. *ACS Energy Letters* **2025**, *10*, 5512−5519.
(30) Yu, T.-Y.; Park, N.-Y.; Kim, H.; Lee, I.-S.; Lee, H.-U.; Kim, K.-H.; Cho, W.; Jung, H.-G.; Chung, K. Y.; Sun, Y.-K. Tuning the Lithium Diffusion Kinetics in Co-Free Layered Cathodes for High-Performance All-Solid-State Batteries. *ACS Energy Letters* **2025**, *10* (5), 2477−2486.
(31) Cao, A.; Manthiram, A. Shape-controlled synthesis of high tap density cathode oxides for lithium ion batteries. *Phys. Chem. Chem. Phys.* **2012**, *14* (19), 6724−6728.
(32) Bielefeld, A.; Weber, D. A.; Janek, J. r. Microstructural modeling of composite cathodes for all-solid-state batteries. *J. Phys. Chem. C* **2019**, *123* (3), 1626−1634.
(33) Shi, T.; Tu, Q.; Tian, Y.; Xiao, Y.; Miara, L. J.; Kononova, O.; Ceder, G. High active material loading in all-solid-state battery electrode via particle size optimization. *Adv. Energy Mater.* **2020**, *10* (1), 1902881.
(34) Jun, S.; Nam, Y. J.; Kwak, H.; Kim, K. T.; Oh, D. Y.; Jung, Y. S. Operando differential electrochemical pressiometry for probing electrochemo-mechanics in all-solid-state batteries. *Adv. Funct. Mater.* **2020**, *30* (31), 2002535.
(35) Jung, S. H.; Kim, U. H.; Kim, J. H.; Jun, S.; Yoon, C. S.; Jung, Y. S.; Sun, Y. K. Ni-rich layered cathode materials with electrochemo-mechanically compliant microstructures for all-solid-state Li batteries. *Adv. Energy Mater.* **2020**, *10* (6), 1903360.
(36) Park, N.-Y.; Lee, H.-U.; Yu, T.-Y.; Lee, I.-S.; Kim, H.; Park, S.-M.; Jung, H.-G.; Jung, Y.-C.; Sun, Y.-K. High-energy, long-life Ni-rich cathode materials with columnar structures for all-solid-state batteries. *Nature Energy* **2025**, *10*, 479.
(37) Hong, S.; Seo, J. K.; Ha, C.; Oh, S.-M.; Kim, Y.-J. Dry-processed bimodal cathode with single-crystalline particles for high-density and high-performance lithium-ion batteries. *J. Power Sources* **2025**, *638*, 236621.
(38) Kirk, T. L.; Evans, J.; Please, C. P.; Chapman, S. J. Modeling electrode heterogeneity in lithium-ion batteries: unimodal and bimodal particle-size distributions. *SIAM Journal on Applied Mathematics* **2022**, *82* (2), 625−653.
(39) Lin, C.-H.; Parthasarathi, S.-K.; Bolloju, S.; Abdollahifar, M.; Weng, Y.-T.; Wu, N.-L. Synthesis of micron-sized LiNi0. *8Co0. 1Mn0. 1O2 and its application in bimodal distributed high energy density Li-ion battery cathodes. Energies* **2022**, *15* (21), 8129.
(40) Hlushkou, D.; Reising, A. E.; Kaiser, N.; Spannenberger, S.; Schlabach, S.; Kato, Y.; Roling, B.; Tallarek, U. The influence of void space on ion transport in a composite cathode for all-solid-state batteries. *J. Power Sources* **2018**, *396*, 363−370.
(41) Banerjee, A.; Wang, X.; Fang, C.; Wu, E. A.; Meng, Y. S. Interfaces and interphases in all-solid-state batteries with inorganic solid electrolytes. *Chem. Rev.* **2020**, *120* (14), 6878−6933.
(42) Minnmann, P.; Schubert, J.; Kremer, S.; Rekers, R.; Burkhardt, S.; Ruess, R.; Bielefeld, A.; Richter, F. H.; Janek, J. Editors' Choice—Visualizing the Impact of the Composite Cathode Microstructure and Porosity on Solid-State Battery Performance. *J. Electrochem. Soc.* **2024**, *171* (6), 060514.
(43) Janek, J.; Zeier, W. G. Challenges in speeding up solid-state battery development. *Nature Energy* **2023**, *8* (3), 230−240.
(44) Gu, J.; Liang, Z.; Shi, J.; Yang, Y. Electrochemo-mechanical stresses and their measurements in sulfide-based all-solid-state batteries: a review. *Adv. Energy Mater.* **2023**, *13* (2), 2203153.
(45) Zhang, R.; Kondrakov, A.; Janek, J.; Brezesinski, T. Timescale identification of electrochemical processes in all-solid-state batteries using an advanced three-electrode cell setup. *Energy Storage Materials* **2025**, *75*, 104000.
(46) Yu, C.-Y.; Choi, J.; Dunham, J.; Ghahremani, R.; Liu, K.; Lindemann, P.; Garver, Z.; Barchiesi, D.; Farahati, R.; Kim, J.-H. Time-resolved impedance spectroscopy analysis of aging in sulfide-based all-solid-state battery full-cells using distribution of relaxation times technique. *J. Power Sources* **2024**, *597*, 234116.

https://doi.org/10.1021/acsenergylett.5c03923
ACS Energy Lett. 2026, 11, 2103−2114

(47) Truong, T. K.; Whang, G.; Huang, J.; Sandoval, S. E.; Zeier, W. G. Probing solid-state battery aging: evaluating calendar vs. *cycle aging protocols via time-resolved electrochemical impedance spectroscopy. Journal of Materials Chemistry A* **2025**, *13* (23), 17261−17270.
(48) Lu, P.; Gong, S.; Wang, C.; Yu, Z.; Huang, Y.; Ma, T.; Lian, J.; Jiang, Z.; Chen, L.; Li, H.; Wu, F. Superior low-temperature all-solid-state battery enabled by high-ionic-conductivity and low-energy-barrier interface. *ACS Nano* **2024**, *18* (10), 7334−7345.
(49) Lee, D.; Shim, Y.; Kim, Y.; Kwon, G.; Choi, S. H.; Kim, K.; Yoo, D.-J. Shear force effect of the dry process on cathode contact coverage in all-solid-state batteries. *Nat. Commun.* **2024**, *15* (1), 4763.
(50) Zhou, K.; Lu, S.; Mish, C.; Chen, Y.-T.; Feng, S.; Kim, J.; Song, M.-S.; Kim, H. A.; Liu, P. Tailored Cathode Composite Microstructure Enables Long Cycle Life at Low Pressure for All-Solid-State Batteries. *ACS Energy Letters* **2025**, *10* (2), 966−974.
(51) Kim, S. Y.; Cha, H.; Kostecki, R.; Chen, G. Composite cathode design for high-energy all-solid-state lithium batteries with long cycle life. *ACS Energy Letters* **2023**, *8* (1), 521−528.
(52) Payandeh, S.; Njel, C.; Mazilkin, A.; Teo, J. H.; Ma, Y.; Zhang, R.; Kondrakov, A.; Bianchini, M.; Brezesinski, T. The effect of single versus polycrystalline cathode particles on all-solid-state battery performance. *Advanced Materials Interfaces* **2023**, *10* (3), 2201806.
(53) Doerrer, C.; Capone, I.; Narayanan, S.; Liu, J.; Grovenor, C. R.; Pasta, M.; Grant, P. S. High energy density single-crystal NMC/Li6PS5Cl cathodes for all-solid-state lithium-metal batteries. *ACS Appl. Mater. Interfaces* **2021**, *13* (31), 37809−37815.
(54) Sham Lal, M.; Saha, A.; Noked, M. Maximizing Areal Capacity in All-Solid-State Li-Ion Batteries Using Single Crystalline Ni-Rich Cathodes and Bromide-Based Argyrodite Solid Electrolytes Under Optimized Stack Pressure. *ACS Appl. Mater. Interfaces* **2025**, *17*, 57046.
(55) Liu, C.; Roters, F.; Raabe, D. Role of grain-level chemo-mechanics in composite cathode degradation of solid-state lithium batteries. *Nat. Commun.* **2024**, *15* (1), 7970.
(56) Liu, B.; Pu, S. D.; Doerrer, C.; Spencer Jolly, D.; House, R. A.; Melvin, D. L.; Adamson, P.; Grant, P. S.; Gao, X.; Bruce, P. G. The effect of volume change and stack pressure on solid-state battery cathodes. *SusMat* **2023**, *3* (5), 721−728.
(57) Kang, J.; Shin, H. R.; Yun, J.; Kim, S.; Kim, B.; Lee, K.; Lim, Y.; Lee, J.-W. Chemo-mechanical failure of solid composite cathodes accelerated by high-strain anodes in all-solid-state batteries. *Energy Storage Materials* **2023**, *63*, 103049.
(58) Naillou, P.; Boulineau, A.; De Vito, E.; Lavanant, E.; Azaïs, P. Direct observation of Li6PS5Cl-NMC electrochemical reactivity in all-solid-state cells. *Energy Storage Materials* **2025**, *75*, 104050.
(59) Park, J.; Kim, K.; Lee, S.; Song, G.; Lee, M.; Jung, H.; Kim, T.; Choi, S. H.; Jo, S.; Lee, K. T. Mechano-Electrochemical and Structural Insights into Composition-Driven Behavior of LiNi1-x-yCoxMnyO2 (0.3< 1-x-y≤ 0.8) Cathodes in Sulfide-Based All-Solid-State Batteries. *Adv. Funct. Mater.* **2025**, No. e17263.
(60) Byeon, Y. S.; Kim, D.; Han, S. A.; Kim, J. H.; Park, M. S. Progress and Challenges in Buffer Layers Between Cathode Materials and Sulfide Solid Electrolytes in All-Solid-State Batteries. *Advanced Energy Sustainability Research* **2024**, *5* (11), 2400135.
(61) Auvergniot, J.; Cassel, A.; Foix, D.; Viallet, V.; Seznec, V.; Dedryvère, R. Redox activity of argyrodite Li6PS5Cl electrolyte in all-solid-state Li-ion battery: An XPS study. *Solid State Ionics* **2017**, *300*, 78−85.
(62) Cha, H.; Yun, J.; Kim, S.; Kang, J.; Cho, M.; Cho, W.; Lee, J.-W. Stabilizing the interface between high-Ni oxide cathode and Li6PS5Cl for all-solid-state batteries via dual-compatible halides. *J. Power Sources* **2024**, *617*, 235157.
(63) Wang, Y.; Wang, Z.; Wu, D.; Niu, Q.; Lu, P.; Ma, T.; Su, Y.; Chen, L.; Li, H.; Wu, F. Stable Ni-rich layered oxide cathode for sulfide-based all-solid-state lithium battery. *EScience* **2022**, *2* (5), 537−545.
(64) Walther, F.; Koerver, R.; Fuchs, T.; Ohno, S.; Sann, J.; Rohnke, M.; Zeier, W. G.; Janek, J. r. Visualization of the interfacial decomposition of composite cathodes in argyrodite-based all-solid-state batteries using time-of-flight secondary-ion mass spectrometry. *Chemistry of materials* **2019**, *31* (10), 3745−3755.
(65) Kim, J.; Choi, W.; Hwang, S. J.; Kim, D. W. Incorporation of Ionic Conductive Polymers into Sulfide Electrolyte-Based Solid-State Batteries to Enhance Electrochemical Stability and Cycle Life. *Energy Environmental Materials* **2024**, *7* (6), No. e12776.
(66) Yun, J.; Shin, H. R.; Hoang, T. D.; Kim, S.; Choi, J. H.; Kim, B.; Jung, H.; Moon, J.; Lee, J.-W. Deciphering the critical degradation factors of solid composite electrodes with halide electrolytes: interfacial reaction versus ionic transport. *Energy Storage Materials* **2023**, *59*, 102787.
(67) Banerjee, A.; Tang, H.; Wang, X.; Cheng, J.-H.; Nguyen, H.; Zhang, M.; Tan, D. H. S.; Wynn, T. A.; Wu, E. A.; Doux, J.-M.; Wu, T.; Ma, L.; Sterbinsky, G. E.; D'Souza, M. S.; Ong, S. P.; Meng, Y. S. Revealing nanoscale solid-solid interfacial phenomena for long-life and high-energy all-solid-state batteries. *ACS Appl. Mater. Interfaces* **2019**, *11* (46), 43138−43145.
(68) Deng, K.; Li, W.; An, P.; Liu, C.; Wu, J.; Wang, R.; Yao, L.; Liu, G. G. Surface to bulk synergistic restructuring of ultrahigh nickel-rich LiNi0. *96Co0. 02Mn0. 02O2 cathode for high-performance sulfide-based all-solid-state batteries. Powder Technology* **2025**, *454*, 120691.
(69) Walther, F.; Randau, S.; Schneider, Y.; Sann, J.; Rohnke, M.; Richter, F. H.; Zeier, W. G.; Janek, J. r. Influence of carbon additives on the decomposition pathways in cathodes of lithium thiophosphate-based all-solid-state batteries. *Chem. Mater.* **2020**, *32* (14), 6123−6136.
(70) Zuo, T.-T.; Walther, F.; Ahmed, S.; Rueß, R.; Hertle, J.; Mogwitz, B.; Volz, K.; Janek, J. r. Formation of an artificial cathode-electrolyte interphase to suppress interfacial degradation of Ni-rich cathode active material with sulfide electrolytes for solid-state batteries. *ACS Energy Letters* **2023**, *8* (3), 1322−1329.
(71) Walther, F.; Strauss, F.; Wu, X.; Mogwitz, B.; Hertle, J.; Sann, J.; Rohnke, M.; Brezesinski, T.; Janek, J. r. The working principle of a Li2CO3/LiNbO3 coating on NCM for thiophosphate-based all-solid-state batteries. *Chem. Mater.* **2021**, *33* (6), 2110−2125.
(72) Qian, L.; Huang, Y.; Dean, C.; Kochetkov, I.; Singh, B.; Nazar, L. Engineering Stable Decomposition Products on Cathode Surfaces to Enable High Voltage All-Solid-State Batteries. *Angew. Chem.* **2025**, *137* (2), No. e202413591.
(73) Manthiram, A.; Knight, J. C.; Myung, S. T.; Oh, S. M.; Sun, Y. K. Nickel-rich and lithium-rich layered oxide cathodes: progress and perspectives. *Adv. Energy Mater.* **2016**, *6* (1), 1501010.
(74) Kim, U.-H.; Park, N.-Y.; Park, G.-T.; Kim, H.; Yoon, C. S.; Sun, Y.-K. High-energy W-doped Li $[Ni_{0.95}Co_{0.04}Al_{0.01}]$ O_2 cathodes for next-generation electric vehicles. *Energy Storage Materials* **2020**, *33*, 399−407.
(75) Ryu, H. H.; Park, K. J.; Yoon, D. R.; Aishova, A.; Yoon, C. S.; Sun, Y. K. Cathodes: Li[Ni0.9Co0.09W0.01]O2: a new type of layered oxide cathode with high cycling stability. *Adv. Energy Mater.* **2019**, *9* (44), 1902698.
(76) Lim, H.; Jun, S.; Song, Y. B.; Bae, H.; Kim, J. H.; Jung, Y. S. Operando electrochemical pressiometry probing interfacial evolution of electrodeposited thin lithium metal anodes for all-solid-state batteries. *Energy Storage Materials* **2022**, *50*, 543−553.
(77) Burkhardt, S.; Friedrich, M. S.; Eckhardt, J. K.; Wagner, A. C.; Bohn, N.; Binder, J. R.; Chen, L.; Elm, M. T.; Janek, J. r.; Klar, P. J. Charge transport in single NCM cathode active material particles for lithium-ion batteries studied under well-defined contact conditions. *ACS Energy Letters* **2019**, *4* (9), 2117−2123.
(78) Ketter, L.; Greb, N.; Bernges, T.; Zeier, W. G. Using resistor network models to predict the transport properties of solid-state battery composites. *Nat. Commun.* **2025**, *16* (1), 1411.

https://doi.org/10.1021/acsenergylett.5c03923
ACS Energy Lett. 2026, 11, 2103−2114